HIGH POWER LASER
SCIENCE AND ENGINEERING

RESEARCH ARTICLE

High-efficiency thin-plate compression of multi-TW Ti:sapphire lasers

Zhaoli Li [1,†], Kainan Zhou[1,2,†], Jie Mu[1], Xiaodong Wang[1], Xiaoming Zeng[1], Zhaohui Wu [1],
Xiao Wang[1], and Yanlei Zuo[1]

[1] *National Key Laboratory of Plasma Physics, Laser Fusion Research Center, China Academy of Engineering Physics, Mianyang, China*

[2] *Sichuan University, Chengdu, China*

Abstract

Nonlinear compression experiments based on multiple solid thin plates are conducted in an ultra-high peak power Ti:sapphire laser system. The incident laser pulse, with an energy of 80 mJ and a pulse width of 30.2 fs, is compressed to 10.1 fs by a thin-plate based nonlinear compression. Significant small-scale self-focusing is observed as ring structures appear in the near-field of the output pulse at high energy. Numerical simulations based on the experimental setup provide a good explanation for the observed phenomena, offering quantitative predictions of the spectrum, pulse width, dispersion and near- and far-field distributions of the compressed laser pulse.

Keywords: nonlinear compression; ultra-high peak power laser; small-scale self-focusing

1. Introduction

Achieving higher laser power has long been a major goal in the development of laser technology as it provides a crucial tool in numerous frontier research fields. To achieve higher power, it is necessary both to increase the laser energy and to compress the laser duration. In conventional chirped-pulse amplification (CPA) technology[1,2], the pulse width of the laser is limited by the gain bandwidth of the gain medium. Optical parametric chirped-pulse amplification (OPCPA) has produced broadband gain for supporting pulses as short as 20 fs, but scaling OPCPA to more than 100 J is still a big challenge[3,4]. Nonlinear compression technology is an emerging laser post-processing technique that compresses the duration of output pulses by broadening the laser spectrum through the self-phase modulation (SPM) effect in a Kerr medium and then compensating for the dispersion generated during the spectrum broadening process using chirped mirrors, grating pairs or prism pairs, therefore obtaining shorter transform-limited pulses. If nonlinear compression technology can be applied to the back-end of CPA/OPCPA laser facilities, the peak power of existing facilities can be increased by several times economically.

Since the basic concept of nonlinear compression was proposed, nonlinear compression technology has been investigated in various Kerr media, including CS_2 liquids[5,6], quartz fibers[7], hollow-core fibers[8], bulk solids[9], inert gases[10] and solid thin plates[11]. Despite extensive research[12,13], the laser energy in those experiments is mostly below the mJ level, and the laser diameter is also below 1 mm. The possibility of utilizing nonlinear compression in ultra-high peak power laser facilities has only been preliminarily explored in an experiment at the PEARL facility in Russia[14-16] and the 100-TW Ti:sapphire laser facility in the Republic of Korea[17], as far as we know. The key limitation to applying nonlinear compression to high-power lasers is the small-scale self-focusing (SSSF)[18,19] effect. To achieve effective spectral broadening, it is necessary to accumulate a large B-integral in the Kerr medium, which comes with severe SSSF, that is, an increase in the amplitude of the spatial harmonic perturbations. SSSF deteriorates the near-field modulation of laser pulses, splits the laser into several strong spots and eventually damages optical components, thus limiting the thickness of the Kerr medium and the compression ratio of the laser pulse, which has not been investigated in previous studies. For this purpose, theoretical and experimental studies on ultra-high
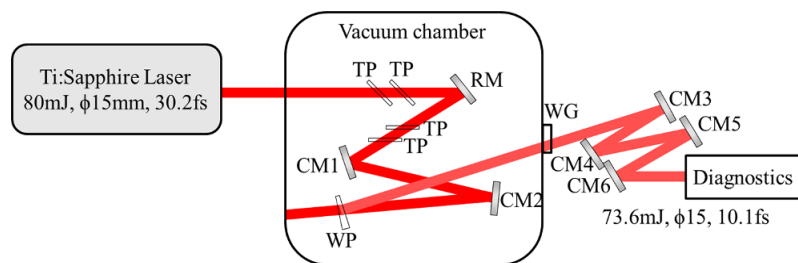

Figure 1. Schematic diagram of the nonlinear compression experimental setup. TP, fused silica plate; RM, reflective mirror; CM, chirped mirror; WP, wedge plate; WG, window glass.

peak power laser nonlinear compression have been carried out based on our 100-TW Ti:sapphire laser facility. Section 2 presents the experimental results on the Ti:sapphire laser, where the spectrum was broadened through Kerr effects of thin solid plates, and the dispersion generated during this process was compensated by two chirped mirrors, resulting in the compression of the laser pulse from 80 mJ, 30.2 fs, 1 Hz to 73.6 mJ, 10.1 fs. Section 3 describes the numerical simulation studies based on the experimental parameters, which closely match the experimental results. Section 4 is the conclusion.

2. Experimental results

The nonlinear compression experiments were conducted in the vacuum target chamber of our 100-TW Ti:sapphire laser facility, which can provide up to 1 J laser energy after grating compression, with a pulse width of 30.2 fs and a diameter of 60 mm. In the experiment, we limited the beam diameter to 15 mm by a soft edge aperture, resulting in 80 mJ energy (i.e., 1.4 TW/cm^2 intensity) reaching the vacuum target chamber. The experimental setup is shown in Figure 1. Four 1 mm thick fused silica plates were used as the Kerr medium. The spectrum broadened laser was then compressed using two chirped mirrors, which provide a total group velocity dispersion of –300 fs^2 to compensate for the dispersion introduced by the thin plates. The compressed laser then passed through a wedge plate that reflects approximately 2.5% of the laser energy. The reflected laser exited the chamber by passing through a 7.5 mm thick fused silica glass window. After exiting the window, the laser pulse was reflected by four additional chirped mirrors, which provided a total dispersion of –300 fs^2 to compensate for the material dispersion introduced by the window glass. Finally, the laser was delivered to the diagnostic instrument. Notice that the optical elements before the wedge plate had a total transmission rate of 92%, which plus the wedge plate make the reflected laser contain approximately 2.3% of the total energy. Meanwhile, the pulse width of the reflected laser was compressed to about one-third by the chirped mirrors in front. So the intensity of the reflected laser when it passed through the window glass was approximately 6.9% of that

of the incident laser when it passed through the thin plates. Therefore, the window glass also had a small contribution to the total B-integral (which should be less than 10% considering that the material dispersion of the window glass quickly broadened the ultrafast reflected laser pulse before it could accumulate enough B-integral).

To reduce the laser reflection, all four plates were placed at Brewster's angle, resulting in a total transmission rate of 92% for the optical path. The spectra of the output pulse with different energies are shown in Figure 2. At low energy, the laser spectrum width is approximately 770–850 nm. When the laser energy increases to 48 mJ, the laser spectrum broadens to 740–900 nm, with two narrow peaks at the edges of the original spectra (around 782 and 850 nm), and the spectral components inside these two peaks gradually transfer to outside these peaks. When the laser energy continues to increase, the spectrum width does not significantly increase, but the amplitude of the two peaks begins to decrease, forming a flatter spectrum. The appearance of two peaks on both sides is attributed to a small amount of residual dispersion in the incident laser pulse, which makes the edge spectral components distribute at the leading and trailing edges of the incident pulse in the time domain. In the experiment, the angle and the distance of the gratings have been finely adjusted to make the second- and the third-order dispersion fully compensated at the same time. However, due to the limited
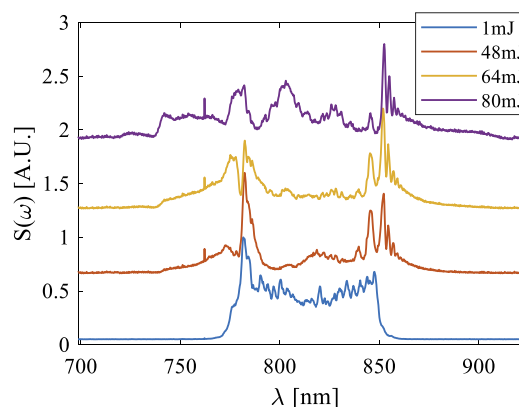

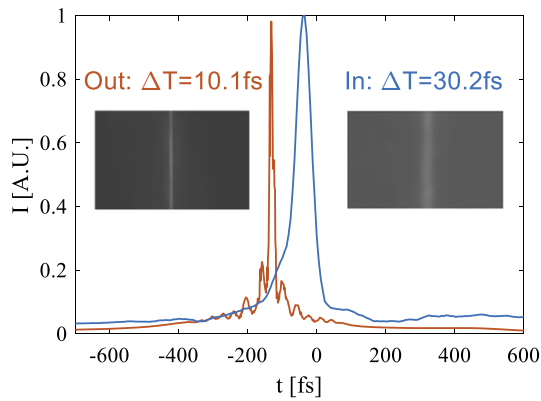**Figure 2.** Spectrum of the output laser pulse with different energies.

Figure 3. Autocorrelation signal of the laser pulse before and after compression.

Figure 4. Pulse widths of the compressed pulse with different laser energies and different group velocity dispersion compensation amounts.

adjustment precision of the gratings, the spectrum still has some second- and third-order dispersion and some high-order dispersion will be generated by the gratings, not to mention that the transmissive materials already generate a lot of high-order dispersion. Therefore, after the compression of the gratings, although most of the spectral components have been gathered in the center region, some marginal spectral components are distributed in the leading and the trailing regions, leading to a smooth edge or a flat pedestal. Recall that the strength of the SPM effect is proportional to the partial derivative of intensity to time and these parts of the spectrum are difficult to broaden, resulting in two peaks remaining in the spectrum. Only at high intensity can these two peaks begin to transfer their energy to other spectral components.

The autocorrelation signals of the laser pulse before and after nonlinear compression are shown in Figure 3. With low energy, the pulse width measured by an autocorrelator is 30.2 fs. With 80 mJ energy, after being compressed by the chirped mirrors, the pulse width is measured to be 10.1 fs. Considering the 92% transmission rate, the peak power increased by 2.75 times. Before nonlinear compression, the autocorrelation curve has a smooth shape with some background. After compression, the autocorrelation curve has more minor structures, indicating that the compressed
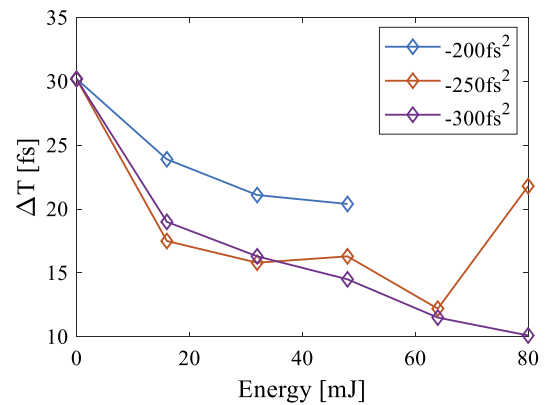
pulse is very close to the transform-limited pulse. The pulse width of the compressed pulse at different laser energies and different group velocity dispersion compensation amounts is shown in Figure 4. It can be seen that when the chirped mirrors provide -200 fs^2 dispersion, the compression effect is limited and the pulse width can only be compressed to 21 fs. When the chirped mirrors provide -250 fs^2 dispersion, the pulse width reaches a minimum value of 12.2 fs with 64 mJ laser energy. However, when the laser energy is increased to 80 mJ, the pulse width increases significantly. A reasonable explanation is that new frequency components were generated when the laser energy increased to 80 mJ, which were not correctly compressed by the chirped mirrors. When the chirped mirrors provide -300 fs^2 dispersion, the pulse width continues to decrease when increasing the laser energy, reaching a minimum value of 10.1 fs with a maximum energy of 80 mJ.

The near-fields of the output pulse with low (5 mJ) and high (64 mJ) energies are shown in Figure 5. The optical path is unchanged between two measurements. With 5 mJ energy, the near-field is relatively uniform; as the laser energy increases, the near-field gradually develops a ring structure, indicating a noticeable SSSF effect at high energy, which will ultimately limit the accumulated B-integral and compression ratio of the laser pulse.
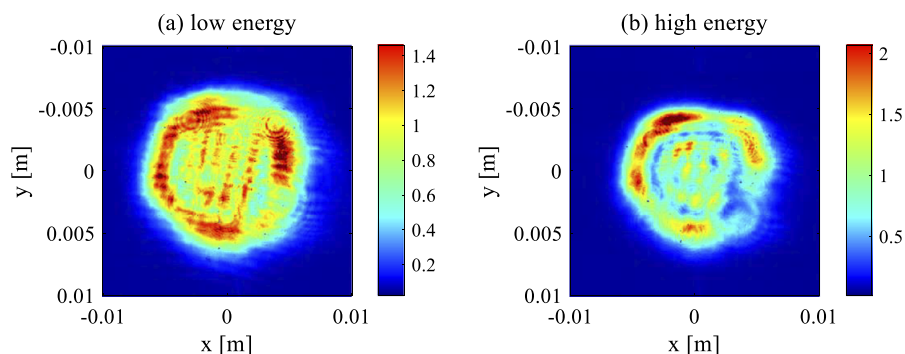

Figure 5. Near-field of the output pulse with (a) low (5 mJ) and (b) high (64 mJ) energies.

To test the stability of the experimental result, the nonlinear compression system worked stably for three days. No visible damage was found in the thin plates or the mirrors when we dismantled the system. The iris diaphragm of the autocorrelator was open when the laser beam entered into the autocorrelator. The autocorrelation signals were vertical lines in the detailed charge-coupled device (CCD) image. We have tried to move the autocorrelator to measure different parts of the laser aperture. The results are very close. No spatio-temporal coupling effect has been observed in the measurement.

3. Simulation results

To explain the experimental results, we use a numerical simulation program to model the laser transmission process. The numerical simulation program is based on the nonlinear Schrödinger equation including the second-, third- and fourth-order dispersion, diffraction, the Raman–Kerr effect, the self-steepening effect and plasma effects[20,21]:

$$\frac{\partial E}{\partial z} = \frac{i}{2k_0} \nabla_\perp^2 E - \frac{ik''}{2} \frac{\partial^2 E}{\partial \tau^2} + \frac{k'''}{6} \frac{\partial^3 E}{\partial \tau^3} + i\frac{k^{(4)}}{24} \frac{\partial^4 E}{\partial \tau^4}$$
$$+ \frac{i\omega_0 n_2}{c} \int_{-\infty}^{t} R\left(t - t'\right) |E|^2 \left(t'\right) dt' E$$
$$- \frac{ik_0}{2n_0^2 \rho_c} \rho E - \frac{\sigma}{2} \rho E - \frac{W\left(|E|^2\right) U_i \left(\rho_{nt} - \rho\right)}{2|E|^2} E, \quad (1)$$

$$R(t) = (1 - f)\, \delta(t) + f \frac{1 + \omega_R^2 \tau_R^2}{\omega_R \tau_R^2} e^{-\frac{t}{\tau_R}} \sin\left(\omega_R t\right), \quad (2)$$

$$\frac{\partial \rho}{\partial t} = W\left(|E|^2\right) \left(\rho_{nt} - \rho\right) + \frac{\sigma |E|^2}{U_i} \rho - \frac{\rho}{\tau_{rec}}. \quad (3)$$

The second-, third- and fourth-order dispersion coefficients for fused silica are set as $k'' = 36\ \text{fs}^2/\text{mm}$, $k''' = 27\ \text{fs}^3/\text{mm}$ and $k^{(4)} = -22\ \text{fs}^4/\text{mm}$. The nonlinear refractive index is $n_2 = 2.4 \times 10^{-20}\ \text{m}^2/\text{W}$, with a Raman effect contribution of $f = 0.15$. The characteristic frequency and relaxation time of the Raman–Kerr effect are $\omega_R = 8.4 \times 10^{13}\ \text{s}^{-1}$ and $\tau_R = 5 \times 10^{-14}\ \text{s}$, respectively. The ionization threshold is $U_i = 7.8$ eV. The absorption cross-section is $\sigma = 5.71 \times 10^{-23}\ \text{m}^2$. The recombination time is $\tau_{rec} = 150$ fs.

We use the alternate direction implicit (ADI) numerical scheme in cylindrical coordinates to calculate the linear terms (the dispersion term and the diffraction term) and adopt the fourth-order Runge-Kutta method to calculate the nonlinear terms. In the simulation, we replace four 1 mm thick thin plates placed at the Brewster's angle with a single 4.9 mm thick plate. To better match the experimental setup, we set the second- and third-order dispersion to zero and calculated the fourth-order dispersion to be $2.22 \times 10^5\ \text{fs}^2$ so the pulse width obtained by fast Fourier transform of the spectrum matches the experimentally measured value. This value is used as the temporal profile of the input laser pulse for the numerical simulation program. When the input laser energy is 48 mJ, the intensity profile and the spectral distribution from the numerical simulation are as shown in Figure 6. It can be seen that the simulated spectral width of 121 nm is close to the experimental measurement of 110 nm. The group velocity dispersion given by the simulation is 208 fs^2. When the dispersion is completely compensated, the laser pulse width is 11.7 fs. In the experiment, the pulse width is 16.3 fs for –250 fs^2 dispersion compensation and 14.5 fs for –300 fs^2 dispersion compensation.

When the laser energy increases to 80 mJ, the intensity profile and the spectral distribution from the numerical simulation are as shown in Figure 7. The simulated spectral width of 152 nm is close to the experimental result of 158 nm. The group velocity dispersion given by the simulation is 206 fs^2, which differs by approximately 100 fs^2 from the optimal experimental value of 300 fs^2. This discrepancy might be due to the membrane dispersion of the broadband reflective mirror (RM), which was not considered in the simulation
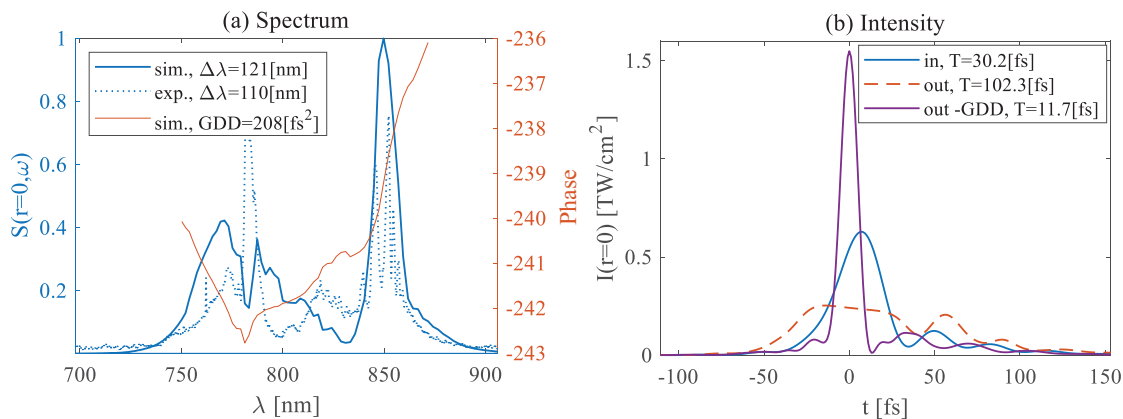

Figure 6. (a) The spectrum distribution of the output pulse with 48 mJ laser energy. Blue solid line, simulation result; blue dotted line, experimental result; red solid line, spectrum phase of the simulation result. (b) The intensity profile of the input and output pulses with 48 mJ laser energy. Blue solid line, input intensity shape; red dashed line, output intensity shape; purple solid line, output intensity shape after compression.

Figure 7. (a) The spectrum distribution of the output pulse with 80 mJ laser energy. Blue solid line, simulation result; blue dotted line, experimental result; red solid line, spectrum phase of simulation result. (b) The intensity profile of the input and output pulses with 80 mJ laser energy. Blue solid line, input intensity shape; red dashed line, output intensity shape; purple solid line, output intensity shape after compression.
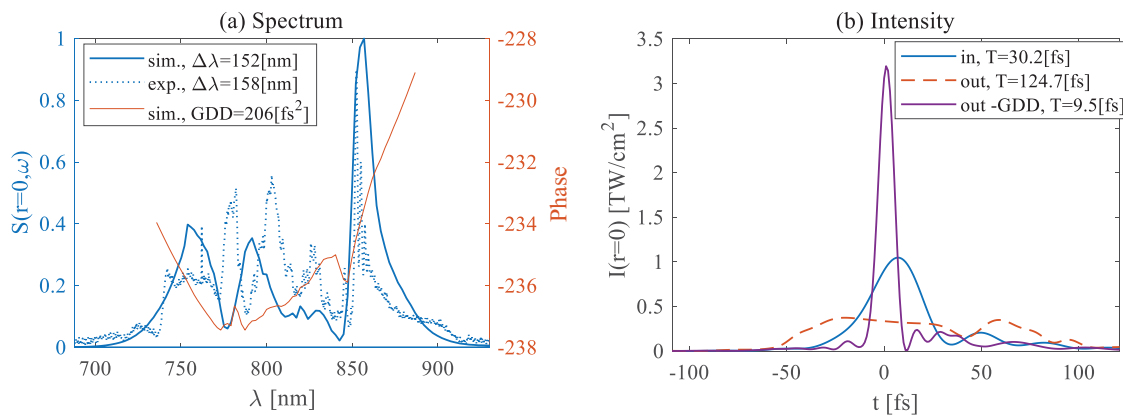
program. In the simulation, when the group velocity dispersion is fully compensated, the pulse width is 9.5 fs. If the higher-order dispersion was further compensated, the laser pulse width could be further compressed to 7.2 fs. In the experiment, the measured pulse width is 10.1 fs, showing good agreement with the simulation.

To simulate the change of the laser near-field in the process of nonlinear compression, we turn to use our three-dimensional (3D) simulation program to calculate the near-field of the laser pulse. The algorithm of the 3D program is the same as that of the two-dimensional (2D) program except that the linear terms are advanced by 3D fast Fourier transform instead of the ADI scheme. We use the near-field distribution of the output pulse with low energy as the near-field distribution of the input pulse in the simulation and set the initial wavefront phase to zero. After passing through four 1.23 mm thick fused silica plates spaced by 50 mm and then traveling 1.85 m in vacuum, the simulated near-field distribution of the output pulse is as shown in Figure 8. The simulation result shows good consistency with the experimental result on the large-scale profile and the modulation amplitude of the near-field distribution, although the

Figure 8. Simulation result of the near-field distribution of the output pulse. The laser energy is 64 mJ and the total optical path is 2 m.

simulated near-field distribution has more high-frequency fluctuations. Considering that the actual near-field of the input pulse is not the same as that of the output pulse with 5 mJ energy, the agreement between the simulation and experimental result is satisfactory.

To simulate the impact of SSSF on the far-field focusing capability caused by the intensity modulation and the wave-front phase distortion, we calculate the fluence distribution of the far-field focal spot before and after nonlinear compression. Under the paraxial approximation and for a broadband laser pulse, the distribution of each spectral component in the focal plane after passing through an ideal lens with focal length f can be calculated using the Fresnel–Kirchhoff integral[22]:

$$S\left(\omega, \overrightarrow{\rho}_0\right) = \frac{1}{\sqrt{2\pi}} \int E\left(t, \overrightarrow{\rho}_0\right) e^{-i\omega t} \mathrm{d}t, \qquad (4)$$

$$S_{\mathrm{f}}\left(\omega, \overrightarrow{\rho}\right) =$$
$$\frac{e^{-ik(\omega)f - ik(\omega)\frac{\rho^2}{2f}}}{i\lambda f} \iint S_0\left(\omega, \overrightarrow{\rho}_0\right) e^{ik(\omega)\frac{\overrightarrow{\rho}_0 \cdot \overrightarrow{\rho}}{f}} \mathrm{d}^2\overrightarrow{\rho}_0. \quad (5)$$

By integrating the spectral components, the far-field fluence distribution F_{f} of the laser pulse at the focal plane can be obtained as follows:

$$F_{\mathrm{f}}\left(\overrightarrow{\rho}\right) = \int \left|S_{\mathrm{f}}\left(\omega, \overrightarrow{\rho}\right)\right|^2 \mathrm{d}\omega, \qquad (6)$$

where $\overrightarrow{\rho}_0$ is the transverse location in the incident plane, f is the focal length and $\overrightarrow{\rho}$ is the transverse location in the focal plane. Setting $f = 1$ m and the initial phase of the input laser to zero, the far-field focal spots of the input and output pulses are as shown in Figures 9(a) and 9(b), respectively. Figure 9(c) shows the focal spot after phase correction. The correction method consists of two steps: firstly, the laser beam is compressed to the limiting pulse
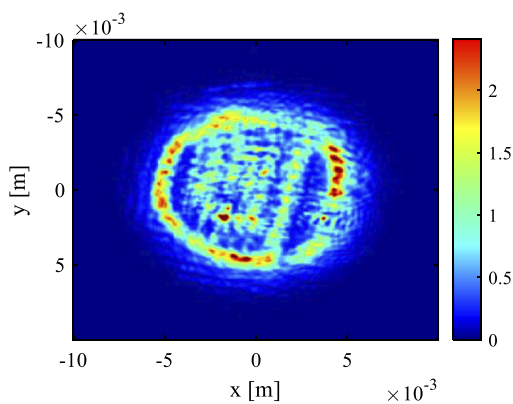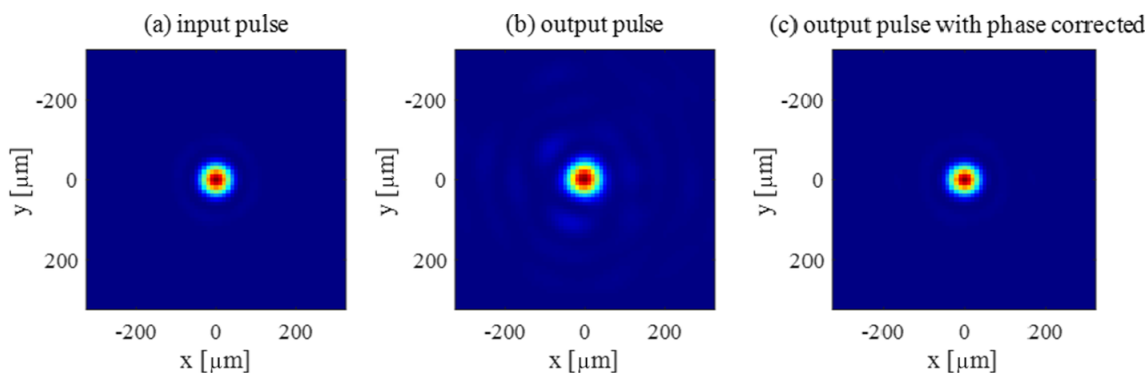
Figure 9. The far-field focal spot of (a) the input pulse, (b) the output pulse and (c) the output pulse with phase correction, using an ideal lens with a focal length of 1 m.

width; then the phase distribution of the cross-section at the time of maximum intensity is used as the reference to compensate for all the time slices of the laser beam, making the beam a plane wave at the time of maximum intensity. The energy concentrations within 200 µm radius for the input pulse, the output pulse and the phase-corrected output pulse are 95.9%, 72.8% and 90.1%, respectively. After passing through the plates, the focusing capability of the laser pulse significantly decreases due to more serious spatial intensity modulation and wavefront phase distortion. The focusing capability can be largely improved by wavefront phase distortion compensation by deformable mirror, but it still suffers a little deterioration compared with the input pulse. It is worth noting that the experimentally observed near-field of the output pulse is smoother than the simulation result, so the far-field focusing capability of the laser pulse after nonlinear compression in the experiment is likely better than the simulation result here. If we calculate the far-field using the experimentally observed near-field and assuming zero wavefront phase, the energy concentration in the far-field spot within 200 µm radius is 93.9%.

As indicated by the experimental and simulation results, a severe SSSF effect may occur in the nonlinear compression process, which should be controlled to achieve high-compression factor nonlinear compression. Generally, there are three methods to suppress SSSF. The first method is inserting transmissive/reflective spatial filters[18,19] into the light path and adjusting the diameter of the pinholes. The high spatial frequency noise produced by SSSF can be hindered by the pinholes, which has been proved as an effective way to control near-field modulation in high-energy laser facilities. The second method is self-filtering[23,24]. A fundamental feature of SSSF is that the propagating angle of the fastest growing noise is proportional to the laser intensity. Because the laser intensity is extremely high in the nonlinear compression, the most dangerous noise components amplified in nonlinear compression are the high spatial frequency noise components, which have large propagating angles and will quickly come out of the beam aperture

when freely propagating in vacuum. For example, for a laser intensity of 1 TW/cm² and Kerr medium of fused silica, a typical propagating angle is 1.5° in free space. Such an angle can make the most dangerous noise components leave the beam aperture with meters of free propagation, which is easy to conduct. It should be noted that in SSSF, the low spatial frequency noise components also have a growth rate. Although the growth rate is low compared to the high spatial frequency noise components, the low spatial frequency noise components cannot be filtered out by reflective spatial filters or self-filtering, and thus must be filtered out by other methods when the B-integral is large. The third method is decreasing the laser near-field modulation by the beam smoothing technique[25,26]. In this scheme, an asymmetric four-grating compressor (AFGC) is used to introduce spatial dispersion into a laser beam. The introduced spatial dispersion redistributes the different spectral components of the laser beam in space, resulting in beam smoothing. As the near-field modulation is suppressed, the allowance of the accumulated B-integral in the nonlinear compression process increases. Simulation works in Ref. [26] show a good effect of the AFGC in the beam smoothing effect, but the efficiency to suppress low and high spatial frequency noises of this method still needs to be explored.

4. Conclusion

The nonlinear compression of ultra-high peak power lasers is demonstrated using a Ti:sapphire laser system. By using four 1 mm thick fused silica plates to broaden the spectrum and two chirped mirrors with a total dispersion of –300 fs² to compress the laser pulse, the incident laser pulse with 80 mJ energy, 15 mm diameter and 30.2 fs pulse width is compressed to 10.1 fs with an output energy of 73.6 mJ. The numerical simulation study based on the experimental parameters effectively explains the observed phenomena, providing quantitative results for the output spectrum, pulse

width, dispersion and near-field distribution. We observe significant SSSF in the high-energy input pulse, leading to a ring-like structure in the near-field of the output pulse. The simulation result shows a similar behavior, with the uniformity of the output pulse slightly worse than the experimental result. SSSF also worsens the far-field focusing capability of the laser pulse, causing a noticeable degradation in far-field energy concentration. An ideal deformable mirror can retrieve the far-field focusing capability to a large extent. For further development of the nonlinear compression technique for ultra-high peak power lasers, it is essential to develop SSSF control techniques and spectrum phase precise control techniques in a broadband laser pulse. Future work will concentrate on the improvement of near-field uniformity, far-field energy concentration, temporal contrast enhancement and high-order dispersion compensation methods.

Acknowledgements

References

1. W. Li, Z. Gan, L. Yu, C. Wang, Y. Liu, Z. Guo, L. Xu, M. Xu, Y. Hang, Y. Xu, J. Wang, P. Huang, H. Cao, B. Yao, X. Zhang, L. Chen, Y. Tang, S. Li, X. Liu, S. Li, M. He, D. Yin, X. Liang, Y. Leng, R. Li, and Z. Xu, Opt. Lett. **43**, 5681 (2018).
2. C. Radier, O. Chalus, M. Charbonneau, S. Thambirajah, G. Deschamps, S. David, J. Barbe, E. Etter, G. Matras, S. Ricaud, V. Leroux, C. Richard, F. Lureau, A. Baleanu, R. Banici, A. Gradinariu, C. Caldararu, C. Capiteanu, A. Naziru, B. Diaconescu, V. Iancu, R. Dabu, D. Ursescu, I. Dancus, C. A. Ur, K. A. Tanaka, and N. V. Zamfir, High Power Laser Sci. Eng. **10**, e21 (2022).
3. X. Zeng, K. Zhou, Y. Zuo, Q. Zhu, J. Su, X. Wang, X. Wang, X. Huang, X. Jiang, D. Jiang, Y. Guo, N. Xie, S. Zhou, Z. Wu, J. Mu, H. Peng, and F. Jing, Opt. Lett. **42**, 2014 (2017).
4. A. Wang, P. Xue, X. Liu, X. Wang, L. Yu, X. Liang, Y. Leng, and R. Li, Opt. Express **32**, 3597 (2024).
5. R. A. Fisher, P. L. Kelley, and T. K. Gustajson, Appl. Phys. Lett. **14**, 140 (1969).
6. A. Laubereau, Phys. Lett. **29**, 539 (1969).
7. C. V. Shank, R. L. Fork, R. Yen, R. H. Stolen, and W. J. Tomlinson, Appl. Phys. Lett. **40**, 761 (1982).
8. M. Nisoli, S. D. Silvestri, and O. Svelto, Appl. Phys. Lett. **68**, 2793 (1996).
9. C. Rolland and P. B. Corkum, J. Opt. Soc. Am. B **5**, 641 (1988).
10. M. Kretschmar, C. Brée, T. Nagy, A. Demircan, H. G. Kurz, U. Morgner, and M. Kovačev, Opt. Express **22**, 22905 (2014).
11. J. Schulte, T. Sartorius, J. Weitenberg, A. Vernaleken, and P. Russbueldt, Opt. Lett. **41**, 4511 (2016).
12. E. A. Khazanov, S. Y. Mironov, and G. Mourou, Phys. Usp. **62**, 1096 (2019).
13. A.-L. Viotti, M. Seidel, E. Escoto, S. Rajhans, W. P. Leemans, I. Hartl, and C. M. Heyl, Optica **9**, 197 (2022).
14. V. Ginzburg, I. Yakovlev, A. Zuev, A. Korobeynikova, A. Kochetkov, A. Kuzmin, S. Mironov, A. Shaykin, I. Shaikin, E. Khazanov, and G. Mourou, Phys. Rev. A **101**, 013829 (2020).
15. V. Ginzburg, I. Yakovlev, A. Kochetkov, A. Kuzmin, S. Mironov, I. Shaikin, A. Shaykin, and E. Khazanov, Opt. Express **29**, 28297 (2021).
16. A. Shaykin, V. Ginzburg, I. Yakovlev, A. Kochetkov, A. Kuzmin, S. Mironov, I. Shaikin, S. Stukachev, V. Lozhkarev, A. Prokhorov, and E. Khazanov, High Power Laser Sci. Eng. **9**, e54 (2021).
17. J. I. Kim, Y. G. Kim, J. Moon Yang, J. W. Yoon, J. H. Sung, S. K. Lee, and C. H. Nam, Opt. Express **30**, 8734 (2022).
18. N. V. Vysotina, N. N. Rosanov, and V. E. Yashin, Opt. Spectrosc. **110**, 973 (2011).
19. S. N. Vlasov, E. V. Koposova, and V. E. Yashin, Quantum Electron. **42**, 989 (2012).
20. A. Couairon and A. Mysyrowicz, Phys. Rep. **441**, 47 (2007).
21. L. Bergé, S. Skupin, R. Nuter, J. Kasparian, and J.-P. Wolf, Rep. Prog. Phys. **70**, 1633 (2007).
22. M. Martyanov, S. Mironov, M. Starodubtsev, A. Soloviev, A. Kochetkov, V. Ginzburg, A. Shaikin, and E. Khazanov, J. Opt. Soc. Am. B **39**, 1936 (2022).
23. S. Mironov, V. Lozhkarev, G. Luchinin, A. Shaykin, and E. Khazanov, Appl. Phys. B: Lasers Opt. **113**, 147 (2013).
24. V. N. Ginzburg, A. A. Kochetkov, A. K. Potemkin, and E. A. Khazanov, Quantum Electron. **48**, 325 (2018).
25. X. Shen, S. Du, W. Liang, P. Wang, J. Liu, and R. Li, Appl. Phys. B **128**, 159 (2022).
26. X. Yang, X. Tang, Y. Liu, J. Bin, and Y. Leng, Opt. Express **31**, 33753 (2023).